



# Mechanical behavior of unidirectional fiber-reinforced polymers under transverse compression: Microscopic mechanisms and modeling

Carlos González, Javier Llorca

## ► To cite this version:

Carlos González, Javier Llorca. Mechanical behavior of unidirectional fiber-reinforced polymers under transverse compression: Microscopic mechanisms and modeling. *Composites Science and Technology*, 2009, 67 (13), pp.2795. 10.1016/j.compscitech.2007.02.001 . hal-00504127

**HAL Id: hal-00504127**

**<https://hal.science/hal-00504127>**

Submitted on 20 Jul 2010

**HAL** is a multi-disciplinary open access archive for the deposit and dissemination of scientific research documents, whether they are published or not. The documents may come from teaching and research institutions in France or abroad, or from public or private research centers.

L'archive ouverte pluridisciplinaire **HAL**, est destinée au dépôt et à la diffusion de documents scientifiques de niveau recherche, publiés ou non, émanant des établissements d'enseignement et de recherche français ou étrangers, des laboratoires publics ou privés.

## Accepted Manuscript

Mechanical behavior of unidirectional fiber-reinforced polymers under transverse compression: Microscopic mechanisms and modeling

Carlos González, Javier LLorca

PII: S0266-3538(07)00071-1  
DOI: [10.1016/j.compscitech.2007.02.001](https://doi.org/10.1016/j.compscitech.2007.02.001)  
Reference: CSTE 3604

To appear in: *Composites Science and Technology*

Received Date: 1 December 2006  
Revised Date: 2 February 2007  
Accepted Date: 2 February 2007

Please cite this article as: González, C., LLorca, J., Mechanical behavior of unidirectional fiber-reinforced polymers under transverse compression: Microscopic mechanisms and modeling, *Composites Science and Technology* (2007), doi: [10.1016/j.compscitech.2007.02.001](https://doi.org/10.1016/j.compscitech.2007.02.001)



This is a PDF file of an unedited manuscript that has been accepted for publication. As a service to our customers we are providing this early version of the manuscript. The manuscript will undergo copyediting, typesetting, and review of the resulting proof before it is published in its final form. Please note that during the production process errors may be discovered which could affect the content, and all legal disclaimers that apply to the journal pertain.

# Mechanical behavior of unidirectional fiber-reinforced polymers under transverse compression: microsocopic mechanisms and modeling

Carlos González and Javier LLorca \*

*Departamento de Ciencia de Materiales, Universidad Politécnica de Madrid &  
IMDEA-Materiales  
E. T. S. de Ingenieros de Caminos. 28040 -Madrid, Spain.*

---

## Abstract

The mechanical behavior of polymer-matrix composites unidirectionally reinforced with carbon or glass fibers subjected to compression perpendicular to the fibers was studied using computational micromechanics. The stress-strain curve was determined by the finite element analysis of a representative volume element of the microstructure idealized as a random dispersion of parallel fibers embedded in the polymeric matrix. The dominant damage mechanisms experimentally observed — interface decohesion and matrix plastic deformation — were included in the simulations, and a parametrical study was carried out to assess the influence of matrix and interface properties on the stress-strain curve, compressive strength, ductility and the corresponding failure modes. It was found that the composite properties under transverse compression were mainly controlled by interface strength and the matrix yield strength in uniaxial compression. Two different fracture modes were identified, depending on whether failure was controlled by the nucleation of interface cracks or by the formation of matrix shear bands. Other parameters, such as matrix friction angle, interface fracture energy or thermo-elastic residual stresses, played a secondary role in the composite mechanical behavior.

---

## 1 Introduction

Unidirectional fiber-reinforced polymers show outstanding specific stiffness and strength along the fiber direction and this has led to a wide range of

---

\* Corresponding author.

*Email address:* jllorca@mater.upm.es (Javier LLorca).

applications as structural materials. Moreover, the fiber and matrix behavior follows very closely the isostrain approximation until the onset of failure and it was possible to develop analytical models to accurately predict the tensile (1; 2; 3) and compressive (4; 5) strength in the fiber direction. Conversely, the mechanical behavior under transverse loading cannot be represented by simplified isostrain or isostress approaches, and micromechanical models capable of predicting failure strength as a function of the constituent properties, volume fraction, shape and spatial distribution are not available. This is an important limitation because the experimental characterization of the lamina properties in the transverse direction is subjected to more uncertainties than in the longitudinal one and, in fact, experimental data are more scarce. In addition, the longitudinal compressive strength is severely affected by the transverse behavior (5; 6), and the development of robust failure criteria for laminates which include the interaction between longitudinal and transverse stresses have to rely on a precise knowledge of the lamina behavior under transverse loading until failure.

Computational micromechanics is emerging as an accurate tool to study the mechanical behavior of composites due to the sophistication of the modelling tools and to the ever-increasing power of digital computers. Within this framework, the macroscopic properties of a composite lamina can be obtained by means of the numerical simulation of the deformation and failure of a representative volume element of the microstructure (7; 8; 9; 10). As compared with the classic homogenization techniques, computational micromechanics presents two important advantages. Firstly, the influence of the geometry and spatial distribution of the phases (i.e. size, shape, clustering, connectivity, etc.) can be accurately taken into account. Secondly, the details of the stress and strain microfields throughout the microstructure are resolved, which leads to precise estimations of the onset and propagation of damage, and to accurate predictions of the failure strength. Recent advances in this area include the analysis of the effect of particle shape (11), particle clustering (12; 13) and the influence of damage (14; 15) on the mechanical behavior of particle-reinforced composites, the prediction of the mechanical behavior of foams and composites whose microstructure was obtained by means of X-ray computer-assisted tomography (16; 17), or the computer simulation of "virtual fracture tests" in fiber-reinforced composites (18; 19).

This strategy is applied in this investigation to analyze the mechanical behavior of a unidirectional fiber-reinforced polymer composite subjected to transverse compression. The composite microstructure was idealized by a random and homogeneous dispersion of parallel, circular elastic fibers embedded in the continuous polymeric matrix. The main deformation and failure mechanisms reported in the literature (namely matrix nonlinear behavior and interface failure) as well as the effect of thermal residual stresses were taken into account in the simulations and a parametrical study was carried out to assess



the influence of these parameters on the stress-strain curve, failure strength, ductility and the corresponding failure modes.

## 2 Experimental background and simulation strategy

The experimental evidence shows that lamina of polymer-matrix composites unidirectionally reinforced with carbon or glass fibers fail under transverse compression along planes parallel to the fibers (20; 21; 22). The angle  $\alpha$  formed between the failure plane and the through-thickness (or perpendicular to the in-plane loading) direction is slightly above  $45^\circ$  and typical values reported are in the range  $50^\circ - 56^\circ$  (23; 21; 24). Significant non-linear deformation was often observed before the maximum load (25; 26), and this behavior was associated to the plastic deformation of the polymeric matrix. This is supported by our observations on the lateral surfaces of a Hexcel 8552 epoxy matrix uniaxially reinforced with 57 vol. % AS4 carbon fibers loaded under transverse compression. Bands of intense plastic deformation in the matrix, inclined at an angle of  $56^\circ$  with respect to the plane perpendicular to the loading axis, appeared before the maximum load was attained (Fig. 1). Damage by interface decohesion developed afterwards around these bands (Fig. 2a) and final fracture occurred by the failure of the matrix in shear, as evidenced by the numerous hackles in the matrix fracture surfaces (Fig. 2b).

These results show that the strength of fiber-reinforced polymers under transverse compression is controlled by two dominant mechanisms, namely the localization of the matrix plastic strain along shear bands and the development of damage by interface decohesion. Both processes (and their interaction) can be taken into account within the framework of computational micromechanics in which composite behavior is analyzed by means of the finite element simulation of a two-dimensional representative volume element (RVE) of the microstructure. The matrix was represented by an isotropic, elasto-plastic solid following the Mohr-Coulomb yield criterion, which assumes that yielding is induced by the shear stresses and that yield stress depends on the normal stress. This model has often been used to describe plastic deformation and failure of polymers (27) and of polymeric matrices in composites (28; 23; 21) as it explains the asymmetry between tensile and compressive yielding and failure in compression along planes forming an angle of  $\approx 50^\circ - 56^\circ$  with respect to the plane perpendicular to the loading axis. Fiber/matrix decohesion was introduced by means of interface elements whose behavior is controlled by a cohesive crack model, a standard technique in the computational micromechanics of composites (29; 30; 31; 32).

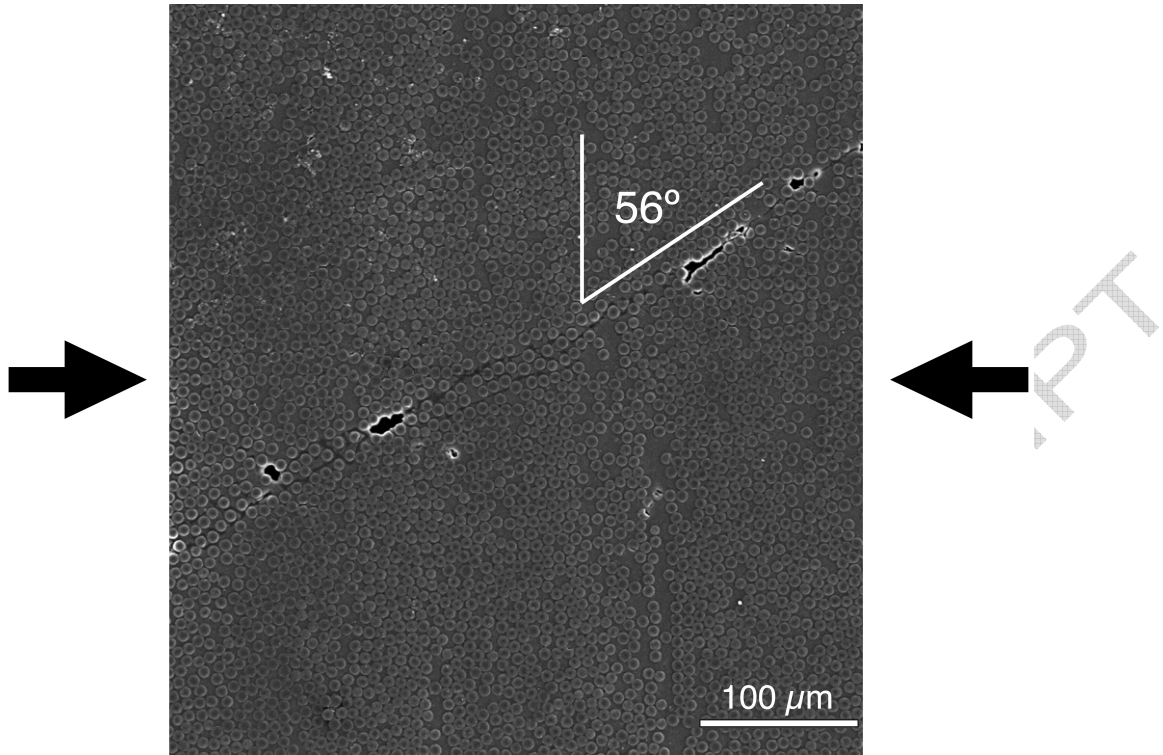


Fig. 1. Scanning electron micrograph of the lateral surface of an AS4/epoxy specimen loaded under transverse compression showing bands of intense plastic deformation in the matrix before the maximum load (24).

### 3 Computational model

#### 3.1 RVE generation and discretization

A square RVE, which contains a random and homogeneous dispersion of circular fibers embedded in the polymeric matrix, was selected to determine the behavior of the composite under transverse loading, following to Brockenbrough *et al.* (33). An important issue in the simulations is the minimum size of the RVE, which should contain all the necessary information about the statistical description of the microstructure and its size should be large enough so that the average properties of this volume element are independent of its size and position within the material. Of course, the critical RVE size depends on the phase and interface properties and spatial distribution, and no estimates were available for our particular problem. It is also known that the accuracy provided by RVEs of a given size can be improved if the results of various realizations are averaged (34). Thus, the compressive strength and ductility for each set of matrix and interface properties was given by the average value of the results obtained from six different fiber distributions in a RVE which included 30 fibers. They were compared in selected cases with those obtained

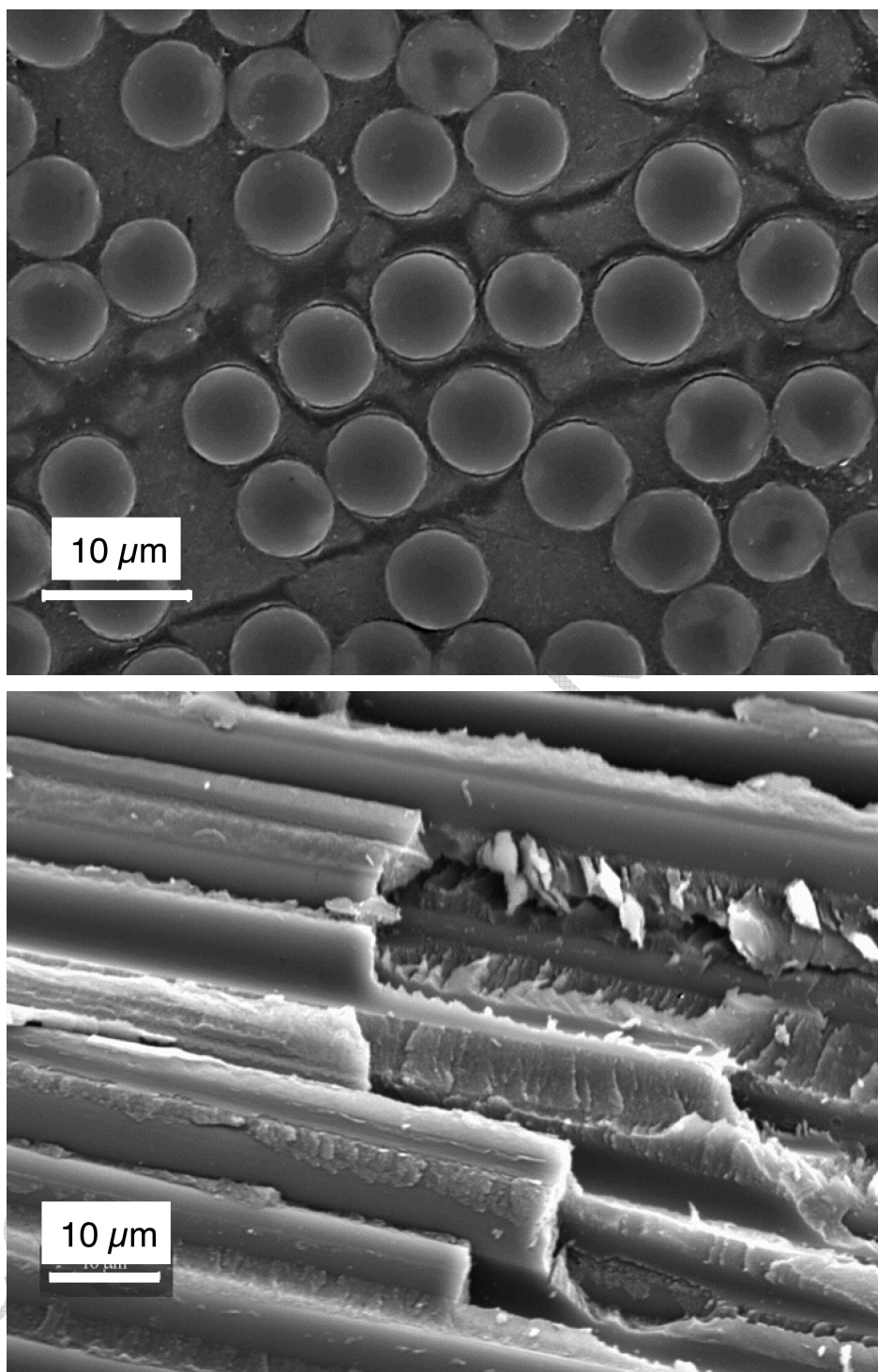


Fig. 2. Scanning electron micrographs of an AS4/epoxy composite loaded under transverse compression (24). (a) Damage by interface decohesion around the matrix shear bands. The loading axis is horizontal. (b) Fracture surface. The presence of numerous hackles in the matrix is indicative of failure by shear.

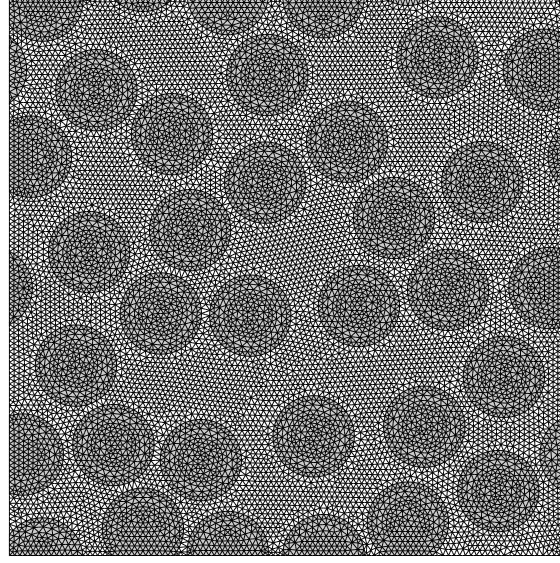


Fig. 3. Fiber distribution and finite element discretization of a representative volume element of the composite with 30 fibers.

with RVEs containing over 70 fibers to ensure that the size of the RVE did not influence significantly the model predictions.

Random and homogeneous dispersions of monosized fibers of radius  $R = 5 \mu\text{m}$  were generated in square RVEs of dimensions  $L_0 \times L_0$  using the modified random sequential adsorption algorithm of Segurado and LLorca (9). It was assumed that the microstructure of the composite was given by a indefinite translation of the RVE along the two coordinate axes and thus the fiber positions within the RVE should keep this periodicity condition. Fiber centers were generated randomly and sequentially, and each new fiber was accepted if the distance between neighboring fiber surfaces was  $> 0.07R$  to ensure an adequate discretization of this region. In addition, the distance between the fiber surface and the RVE edges should be  $> 0.1R$  to avoid distorted finite elements during meshing. Fibers intersecting the RVE edges were split into an appropriate number of parts and copied to the opposite sides of the square RVE to create a periodic microstructure. New fibers were added until the desired volume fraction of 50 % was reached. An example of the fiber distribution an RVE with 30 fibers is shown in Fig. 3. The RVE was automatically meshed using 6-node isoparametric modified triangles (CPE6M in Abaqus Standard(35)) with integration at three Gauss points and hourglass control. Special care was taken to obtain a very fine and homogeneous discretization throughout the RVE to resolve the plastic shear bands in the matrix during deformation (Fig. 3).

**Table 1**

**Thermo-elastic constants of the fibers and the matrix (38)**

$E_f$	$\nu_f$	$\alpha_f$	$E_m$	$\nu_m$	$\alpha_m$
(GPa)		( $10^{-6}\text{K}^{-1}$ )	(GPa)		( $10^{-6}\text{K}^{-1}$ )
40	0.25	10	4	0.35	50

### 3.2 Finite element and material models

Periodic boundary conditions were applied to the edges of the RVE because the continuity between neighboring RVEs (which deform like jigsaw puzzles) is maintained and, in addition, because the effective behavior derived under these conditions is always bounded by those obtained under imposed forces or displacements (36; 37). Let  $X_1$  and  $X_2$  stand as the Cartesian coordinate axes parallel to the RVE edges and with origin at one corner of the RVE. The periodic boundary conditions can be expressed in terms of the displacement vectors  $\vec{U}_1$  and  $\vec{U}_2$  which relate the displacements between opposite edges according to

$$\vec{u}(0, X_2) - \vec{u}(L_0, X_2) = \vec{U}_1 \quad (1)$$

$$\vec{u}(X_1, 0) - \vec{u}(X_1, L_0) = \vec{U}_2. \quad (2)$$

Uniaxial compression along the  $X_2$  axis is imposed with  $\vec{U}_2 = (0, -\delta)$  and  $\vec{U}_1 = (u_1, 0)$ .  $\delta$  stands for the imposed displacement in the loading direction and  $u_1$  is computed from the condition that the average stresses on the edges perpendicular to the loading axis should be 0. Mathematically,

$$\int_0^L \vec{t} dX_2 = 0 \quad \text{on} \quad X_1 = 0 \quad (3)$$

where the integral stands for the resultant forces acting on the edge  $X_1 = 0$  due to the traction vector  $\vec{t}$ . The logarithmic strain along the loading axis was given as  $\epsilon = \ln(1 + \delta/L_0)$  and the corresponding true stress on the edge was computed as the resultant force divided by the actual cross-section.

Simulations were carried out with Abaqus/Standard (35) under plane strain conditions and within the framework of the finite deformations theory with the initial unstressed state as reference. Fibers were modeled as linear, thermo-elastic and isotropic solids. The thermo-elastic constants given in Table 1 are intermediate between those of glass and C fibers in the plane perpendicular to the fiber axis. The polymeric matrix was assumed to behave as an isotropic,

thermo-elasto-plastic solid, and the thermo-elastic constants (typical of an epoxy matrix) are also given in Table 1. Plastic deformation was governed by the Mohr-Coulomb criterion and the total matrix strain was given by the addition of the thermo-elastic and plastic strain components. The Mohr-Coulomb criterion assumes that yielding takes place when the shear stress acting on a specific plane,  $\tau$ , reaches a critical value, which depends on the normal stress  $\sigma$  acting on that plane. This can be expressed as

$$\tau = c - \sigma \tan \phi \quad (4)$$

where  $c$  and  $\phi$  stand, respectively, for the cohesion and the friction angle, two materials parameters which control the plastic behavior of the material. Physically, the cohesion  $c$  represents the yield stress under pure shear while the friction angle takes into account the effect of the hydrostatic stresses.  $\phi = 0$  reduces the Mohr-Coulomb model to the pressure-independent Tresca model while  $\phi = 90^\circ$  leads to "tension cut-off" Rankine model. The value of both parameters for an epoxy can be assessed from its tensile and compressive strengths,  $\sigma_{mt}$  and  $\sigma_{mc}$ , according to

$$\sigma_{mt} = 2c \frac{\cos \phi}{1 + \sin \phi} \quad \text{and} \quad \sigma_{mc} = 2c \frac{\cos \phi}{1 - \sin \phi} \quad (5)$$

The fracture surface of a solid which follows the Mohr-Coulomb criterion and it is subjected to uniaxial compression forms an angle  $\alpha$  with plane perpendicular to the loading axis, which is related to the friction angle  $\phi$  by

$$\alpha = 45^\circ + \phi/2 \quad (6)$$

Typically  $50^\circ < \alpha < 60^\circ$  in epoxy matrices (23; 21; 24), and thus  $\phi$  is in the range  $10^\circ - 30^\circ$ . Once  $\phi$  was fixed for a given simulation, the corresponding cohesion  $c$  was computed from equation (5) assuming that the matrix tensile strength was 60 MPa (38). If not indicated otherwise, the simulations presented in this paper used  $\phi = 15^\circ$  to represent the matrix behavior, which corresponds to a cohesion  $c$  of 39.1 MPa. The corresponding values on the matrix tensile and compressive strength are, respectively, 60 MPa and 101.9 MPa.

The yield surface of the Mohr-Coulomb model, written in terms of the maximum and minimum principal stresses ( $\sigma_I$  and  $\sigma_{III}$ ), is given by

$$F(\sigma_I, \sigma_{III}) = (\sigma_I - \sigma_{III}) + (\sigma_I + \sigma_{III}) \sin \phi - 2c \cos \phi = 0 \quad (7)$$

and it was assumed that  $c$  and  $\phi$  were constant and independent of the accumulated plastic strain. A non-associative flow rule was used to compute the directions of plastic flow in the stress space and the corresponding potential flow  $G$  was expressed as

$$G = \frac{4(1 - e^2) \cos^2 \Theta + (2e - 1)^2}{2(1 - e^2) \cos \Theta + (2e - 1) \sqrt{4(1 - e^2) \cos^2 \Theta + 5e^2 - 4e}} \frac{3 - \sin \phi}{6 \cos \phi} \quad (8)$$

in which  $e = (3 - \sin \phi)/(3 + \sin \phi)$  and  $\Theta$  is obtained from

$$\Theta = \frac{1}{3} \arccos \left\{ \frac{J_3}{J_2} \right\}^3 \quad (9)$$

where  $J_2$  and  $J_3$  are, respectively, the second and the third invariants of the deviatoric stress tensor. More details about the numerical implementation of the Mohr-Coulomb model can be found in (39; 40).

The progressive interface decohesion upon loading was simulated by 4-node isoparametric linear interface elements (COH2D4 in (35)) inserted at the fiber/matrix interface. The mechanical behavior of these elements was expressed in terms of a traction-separation law which relates the displacement jump across the interface with the traction vector acting upon it. The initial response was linear in absence of damage and, therefore, the traction-separation law can be written as

$$t_n = K \delta_n \quad \text{and} \quad t_s = K \delta_s \quad (10)$$

where  $t_n$ ,  $t_s$ ,  $\delta_n$  and  $\delta_s$  stand for the normal and tangential tractions and displacement jumps across the interface respectively. An elastic stiffness of  $K = 10^8$  GPa/m was selected for the interface, which was large enough to ensure the displacement continuity at the interface and to avoid any modification of the stress fields around the fibers in the absence of damage. The linear behavior ends at the onset of damage, which is dictated by a maximum stress criterion expressed mathematically as

$$\max \left\{ \frac{\langle t_n \rangle}{N}, \frac{t_s}{S} \right\} = 1 \quad (11)$$

in which  $\langle \rangle$  stand for the Macaulay brackets, which return the argument if positive and zero otherwise, to impede the development of damage when

the interface is under compression, and  $N$  and  $S$  are the normal and tangential interfacial strengths which were assumed to be the equal for simplicity ( $N = S$ ). Once the damage begins, the stress transferred through the crack is reduced depending on the interface damage parameter  $d$ , which evolves from 0 (in the absence of damage) to 1 (no stresses transmitted across the interface), as shown in Fig. 4. The corresponding traction-separation law is expressed by

$$\begin{aligned} t_n &= (1 - d)K\delta_n & \text{if } \delta_n > 0 \\ t_n &= K\delta_n & \text{if } \delta_n \leq 0 \\ t_s &= (1 - d)K\delta_s \end{aligned} \quad (12)$$

The evolution of the damage parameter is controlled by an effective displacement,  $\bar{\delta}$ , defined as the norm of the displacement jump vector across the interface as

$$\bar{\delta} = \sqrt{\langle \delta_n \rangle^2 + \delta_s^2}, \quad (13)$$

and  $d$  depends on the maximum effective displacement at the interface attained during the loading history at each material integration point  $\bar{\delta}^{max}$  according to

$$d = \frac{\bar{\delta}^f(\bar{\delta}^{max} - \bar{\delta}^0)}{\bar{\delta}^{max}(\bar{\delta}^f - \bar{\delta}^0)} \quad (14)$$

where  $\bar{\delta}^0$  and  $\bar{\delta}^f$  stand for the effective displacement at the onset of damage ( $d = 0$ ) and when the interface has failed completely ( $d = 1$ ), respectively. In this cohesive model, the energy necessary to completely break the interface is always equal to  $\Gamma$ , the interface fracture energy, regardless of the loading path. If not indicated otherwise, the interface fracture energy in the simulations presented below was 100 J/m<sup>2</sup>, a reasonable value for C and glass fibers embedded in a polymeric matrix (41).



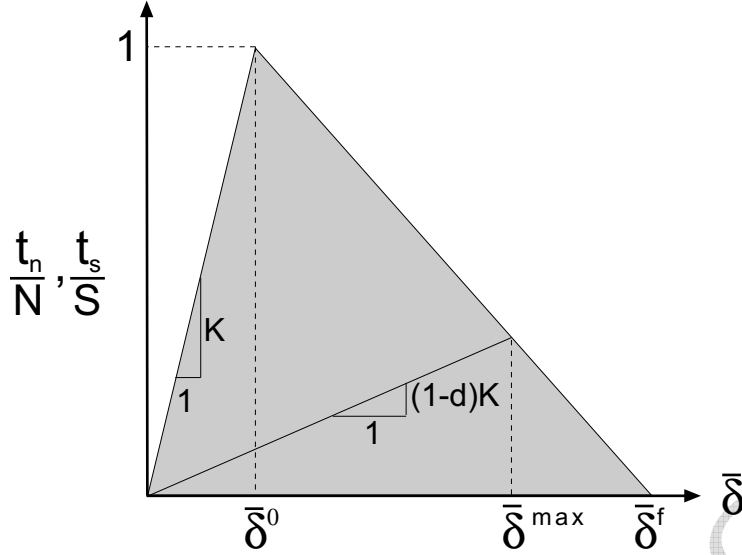


Fig. 4. Schematic of the traction-separation law which governs the behavior of the interface elements.

## 4 Results

### 4.1 Validation of the RVE size

Most of the results presented in this paper were obtained by the numerical simulation of RVEs containing 30 fibers. The influence of the actual position of the fibers within the RVE on the mechanical response was analyzed by comparing the results obtained with six different fiber realizations for the typical values of the matrix and fiber properties given previously and two sets of interface properties corresponding to very weak ( $N = 0.1c$ ) and perfect interfaces, respectively. The corresponding (compression) stress-strain curves are plotted in Fig. 5, together with those computed with an RVE which included 70 fibers. All the simulations were practically superposed in the elastic regime; divergences arose at the onset of matrix plastic deformation and increased in the composite with weak interfaces beyond the maximum load. These results are in agreement with previous numerical studies, which showed that the minimum size of the RVE increases with the mismatch between the phase properties (e.g. at the elasto-plastic transition) and especially with the localization of the deformation due to plastic flow and/or damage (42; 10). Nevertheless, the dispersion among the stress-strain curves was limited and the curve obtained by averaging the six simulations was very close to that computed with an RVE with 70 fibers for both sets of material properties.

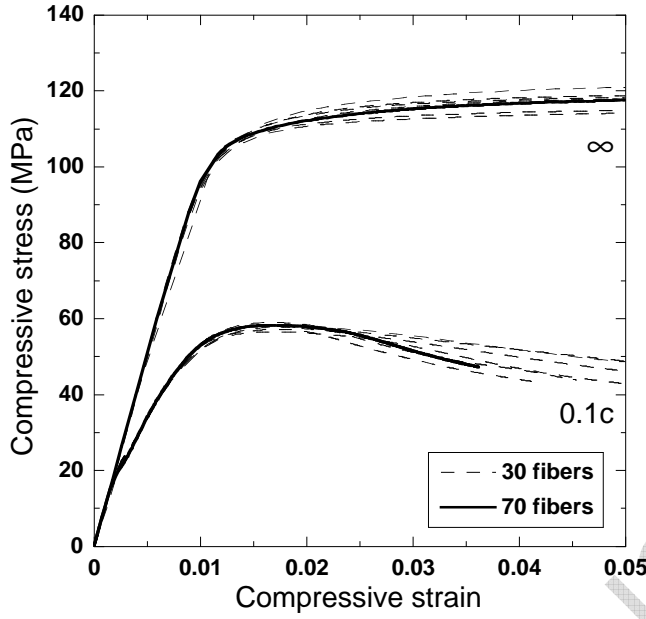


Fig. 5. Compressive stress-strain curves for six different fiber realizations in RVEs with 30 fibers (broken line) and one fiber realization in an RVE with 70 fibers (solid line). The two sets of curves are representative of materials with very strong ( $= \infty$ ) or very weak ( $= 0.1c$ ) fiber/matrix interfaces.

#### 4.2 Influence of the interface strength

The stress-strain curve under transverse compression is plotted in Fig. 6 for composite materials whose interface strength varied from  $N = 0.1c$  to infinity. The matrix friction angle was  $15^\circ$  ( $c = 39.1$  MPa) and the interfacial fracture energy was  $100$  J/m<sup>2</sup> in all cases. Each curve is the average of six different realizations with an RVE with 30 fibers and the error bars stand for the standard deviation of the simulations, which was negligible up to the maximum load and remained small afterwards. The initial composite stiffness was not affected by the interface strength but the composites with low interfacial strength ( $N < c$ ) departed early from the linear behavior due to the nucleation of interface cracks. In isolated fibers, the cracks nucleated at the points equidistant from the poles and the equator (latitudes  $45^\circ\text{N}$  and  $45^\circ\text{S}$ ), where the interfacial shear stress was maximum. They propagated towards the equator and merged. The stress concentrations at the tip of the interface cracks induced the formation of very short shear bands in the matrix linking up interface cracks in neighboring fibers, and the maximum strength was attained at this point (Fig. 7a). Further deformation led to formation of interfacial voids and to the localization of the strain in the matrix in shear bands whose path was dictated by the position of the voids which grew from the interface cracks

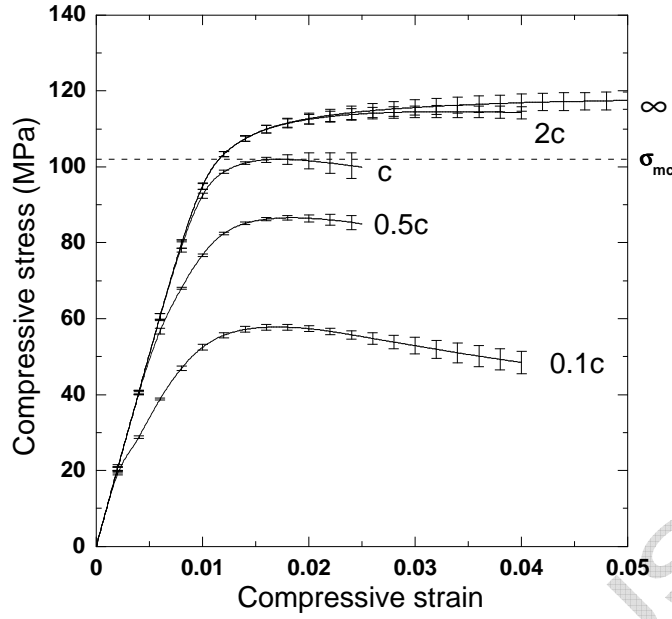


Fig. 6. Influence of the interface strength  $N$  on the mechanical response under transverse compression. The error bars stands for the standard deviation of six simulations. The figure next to each curve stands for the interface strength. The broken horizontal line represents the compressive strength of the epoxy matrix.

(Fig. 7b).

On the contrary, composites without interface decohesion presented a linear behavior up to compressive stresses very close to the strength of the epoxy matrix in uniaxial compression,  $\sigma_{mc}$ . This linear regime was followed by a plastic response with very little hardening as the localization of the plastic strain in the matrix led to the formation of shear bands which percolated the entire RVE (Fig. 8). It is worth noting that the angle between the shear bands and the plane perpendicular to the loading axis was very close to  $45^\circ + \phi/2 = 52.5^\circ$ , the theoretical one for the matrix alone, regardless of the actual fiber distribution, and this indicates that the composite strength was determined by the propensity of the matrix to form shear bands.

The behavior of the composite with an intermediate interfacial strength ( $N = c$ ) was initially similar to that of the materials with high interfacial strength, and the pattern of plastic deformation in the matrix at the point of maximum stress showed the incipient development of shear bands oriented at  $52.5^\circ$  (Fig. 9a). However, final fracture occurred by the development of a single shear band, slightly misoriented with respect to the theoretical angle, whose orientation was dictated by the linking up of interface cracks in adjacent fibers (Fig. 9b). This fracture pattern is very similar to that observed in Fig. 2(a),

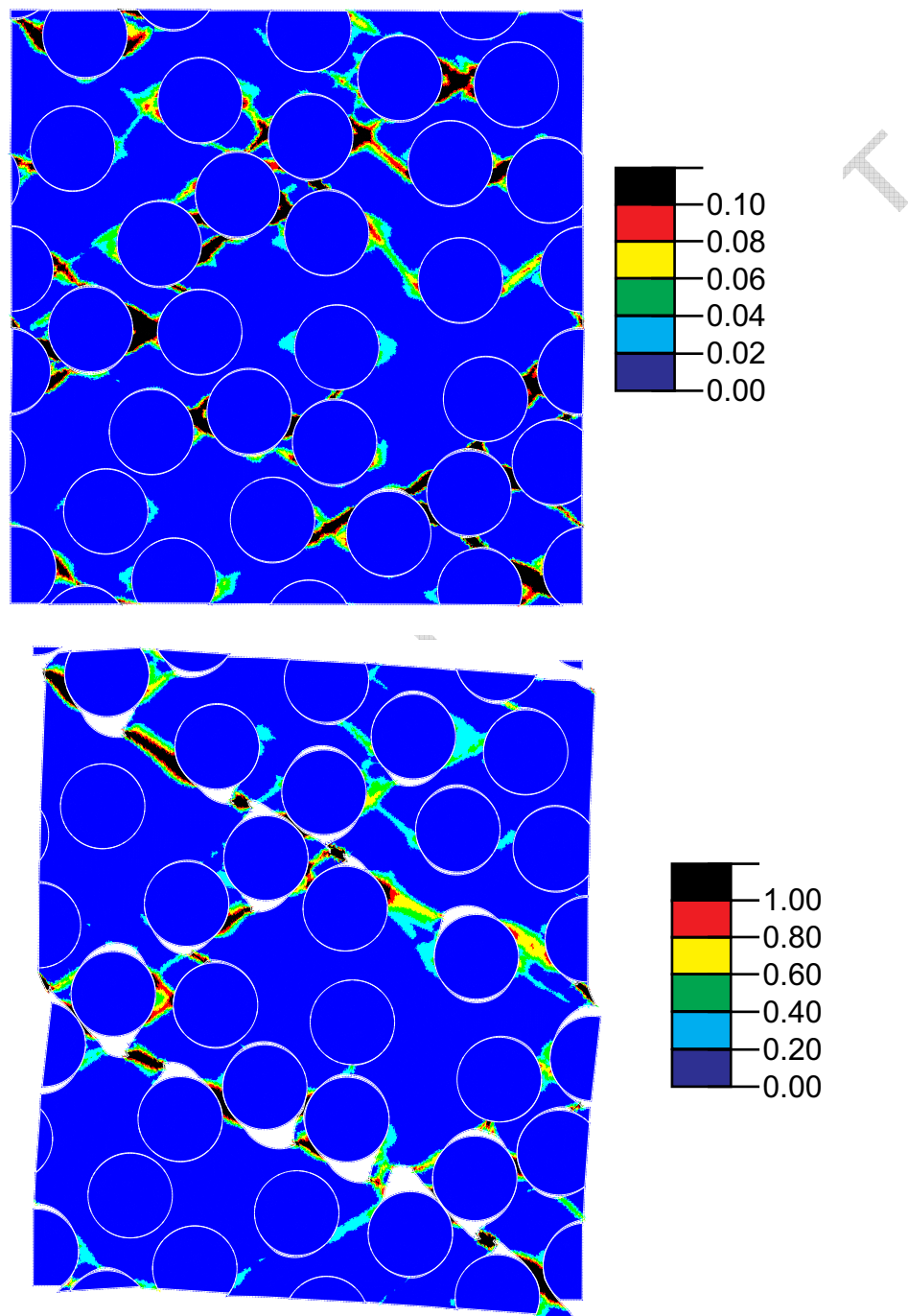


Fig. 7. Contour plot of the accumulated plastic strain in the matrix in the composite with low interfacial strength ( $N = 0.1c$ ). (a)  $\epsilon = -1.7\%$  corresponding to the maximum strength. (b)  $\epsilon = -4\%$ . The loading axis is horizontal. Notice that the strain values in legend (b) are ten times higher than in (a).

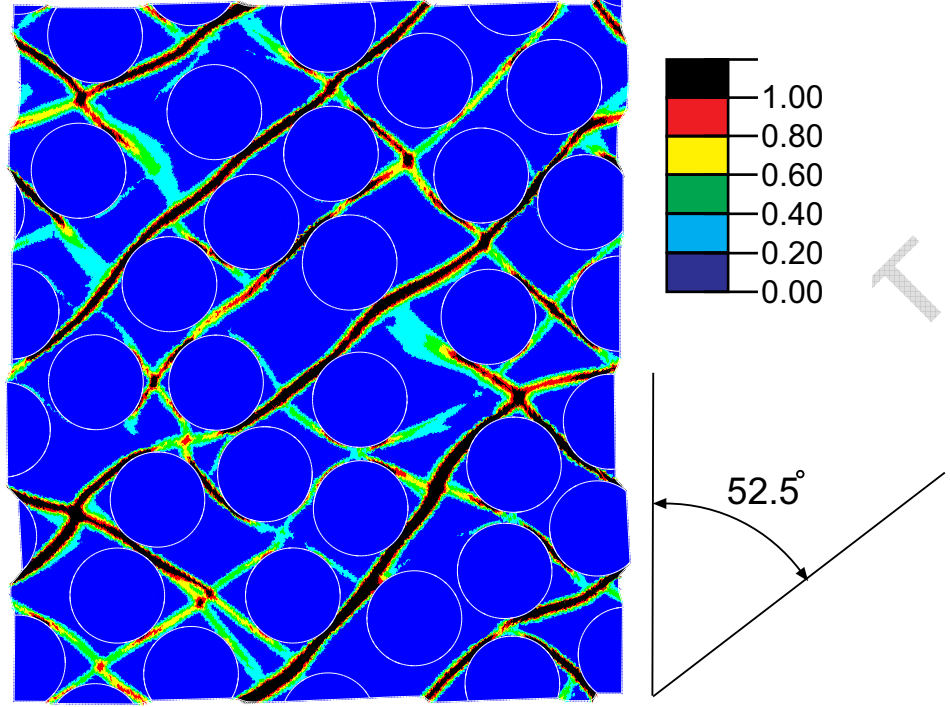


Fig. 8. Contour plot of the accumulated plastic strain in the matrix in the composite without interface decohesion ( $N = \infty$ ) at  $\epsilon = -7\%$ . The loading axis is horizontal.

in which the matrix shear band is surrounded by interface cracks and points to a failure process in three steps: incipient development of shear bands in the matrix channels between the fibers, nucleation of interface cracks, and final localization of the deformation in the matrix in one dominant shear band.

The transverse compressive strength,  $Y_C$ , is given by the maximum of each curve in Fig. 6, and the overall effect of interface strength in the transverse compressive strength,  $Y_C$ , is plotted in Fig. 10. Failure is controlled by the matrix plastic deformation if  $N/c \geq 2$  and the reinforcing effect of the stiff fibers increased the composite strength approximately 10% over the matrix flow stress in compression. The composite strength decreases rapidly with the interfacial strength as the stress concentrations associated with interface cracks favor the onset of plastic deformation in the matrix and the nucleation of shear bands at lower stresses. It is interesting to note that predictions of the micromechanics simulations are in good agreement with experimental results for epoxy-matrix composites reinforced with either glass or carbon fibers (Fig. 10). Experimental values of the matrix and composite properties under transverse compression were obtained from (38); information of the interface strength for both composite systems was not available in this reference and the experimental data in (43) for C/epoxy and in (44) for glass/epoxy were used. Thus, although the actual interface strength is not known, it is evident that the model predictions for the transverse compressive strength and the failure micromechanisms (Figs. 1 and 2) support the validity of the current

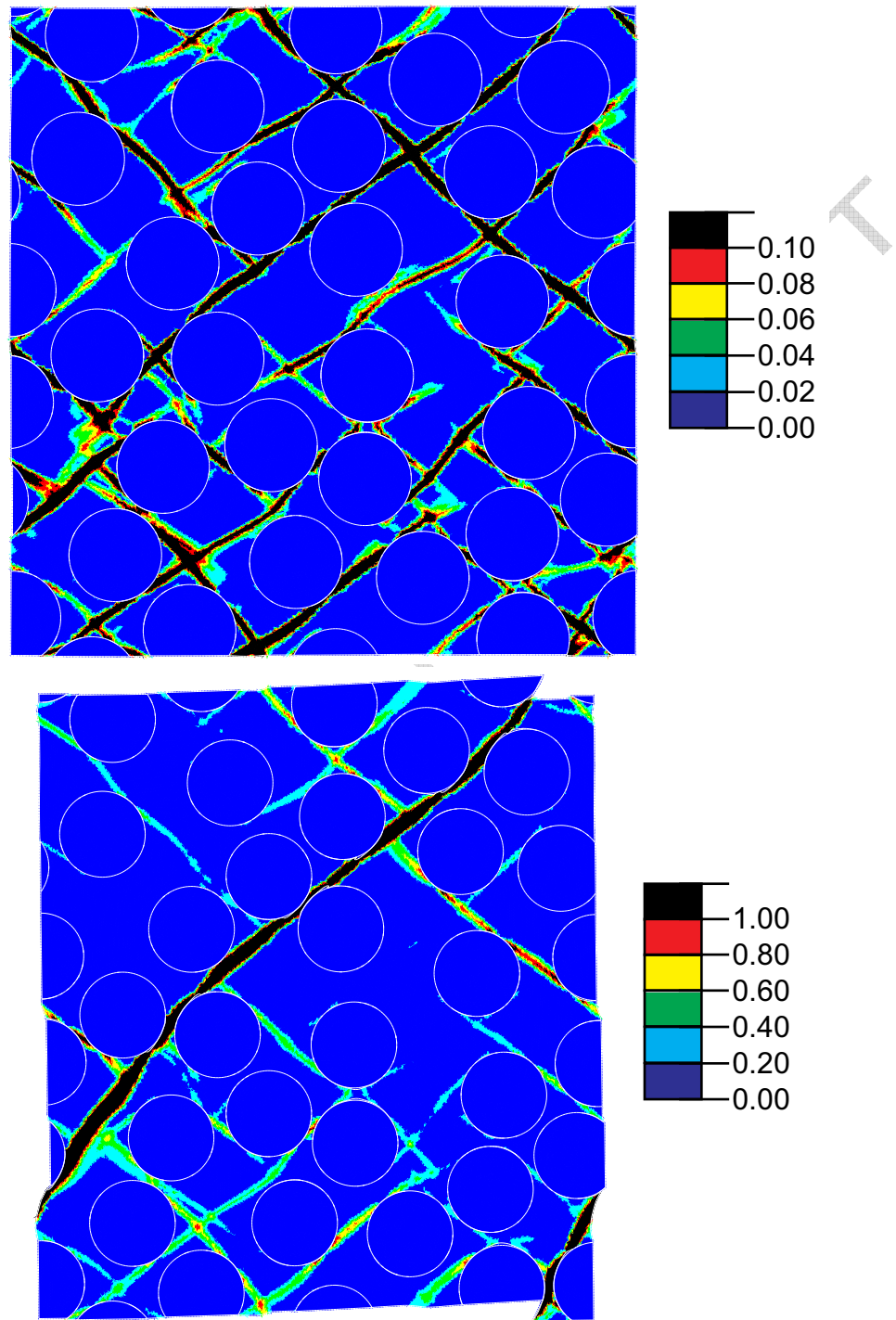


Fig. 9. Contour plot of the accumulated plastic strain in the matrix in the composite with intermediate interfacial strength ( $N=c$ ). (a)  $\epsilon = -1.7\%$  corresponding to the maximum strength. (b)  $\epsilon = -2.5\%$ . The loading axis is horizontal. Notice that the strain values in legend (b) are ten times higher than in (a).

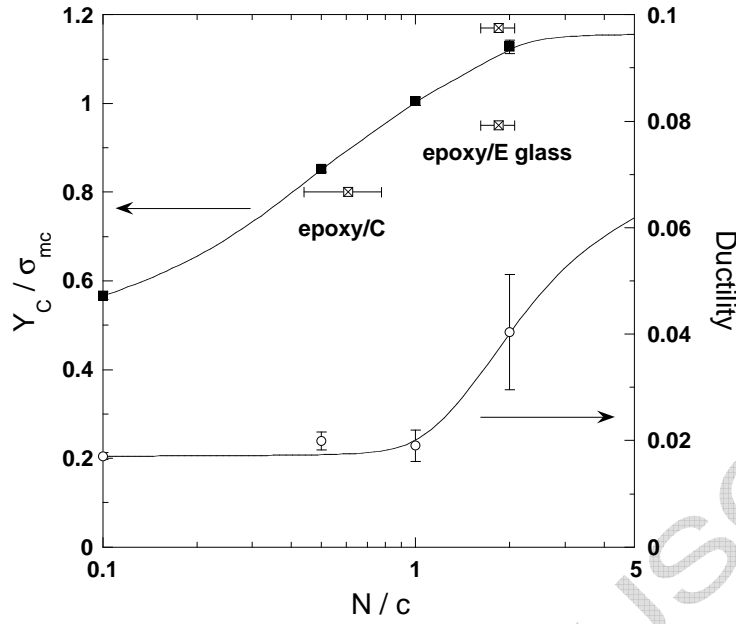


Fig. 10. Influence of the interface strength (normalized by the cohesion of the matrix  $c$ ) in the transverse compressive strength,  $Y_C$  (normalized by the yield strength of the matrix in compression,  $\sigma_{mc}$ ) and in the ductility, represented by the strain at  $Y_C$ . The error bars stand for the standard deviation of the six simulations with different RVEs.

approach to simulate the mechanical behavior of unidirectional PMC.

The data in Fig. 10 also include the influence of the interface properties in the strain at  $Y_C$ , which stands for a rough approximation of the composite ductility under transverse compression. The ductility values presented more scatter (particularly for large interface strengths, in which the stress-strain curve is very flat near  $Y_C$ ) but they clearly show the differences between interface- and matrix-dominated fracture. The former occurred when  $N < c$  and it was characterized by a brittle behavior, while the latter was dominant if  $N \geq 2c$  and led to much higher strain to failure (4-6%) controlled by the plastic deformation of the matrix.

#### 4.3 Influence of the interface fracture energy

The influence of the interface fracture energy on the mechanical behavior in transverse compression is plotted in Fig. 11. Simulations were performed with the same RVE (whose behavior was very similar to the average of six simulations with different RVEs) and three interface fracture energies: 100 J/m<sup>2</sup> (the baseline value), 10 J/m<sup>2</sup> and 1000 J/m<sup>2</sup>, while the interface strength

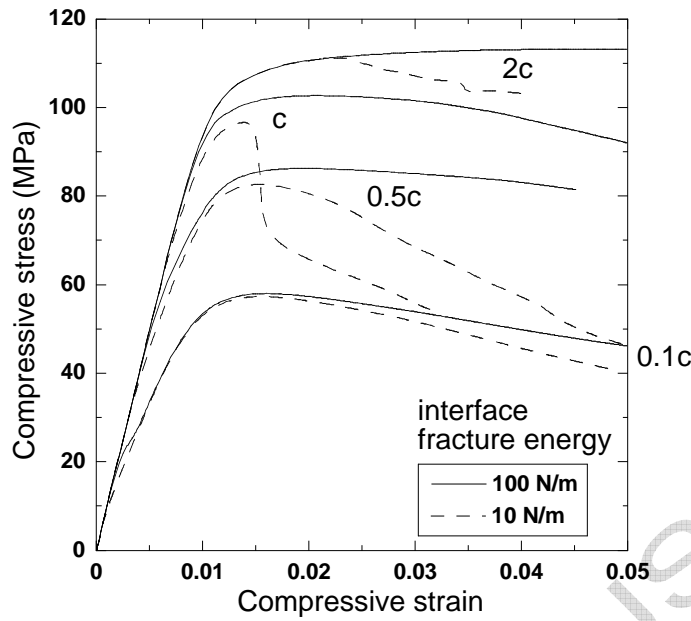


Fig. 11. Influence of the interface fracture energy on the stress-strain curve under transverse compression for different values of the interface strength.

was systematically varied from  $0.1c$  up to  $2c$ . For a given value of the interface strength, the variations in the fracture energy modified the effective interface displacement at failure,  $\bar{\delta}^f$  (Fig. 4), leading to more brittle or more ductile behaviors. The rest of the fiber and matrix properties were those indicated in section 3. The stress-strain curves of the materials with interface fracture energies of 10 and 100 J/m<sup>2</sup> are plotted in Fig. 11. The curves corresponding to the materials with interface fracture energies of 1000 J/m<sup>2</sup> were practically superposed to those with 100 J/m<sup>2</sup> up to the maximum stress in all cases, even though the fracture energies differed in one order of magnitude, and the differences beyond that point were minimum. They are not plotted in Fig. 10 for sake of clarity. Brittle fiber/matrix interfaces (which are represented by the curves obtained with  $\Gamma = 10$  J/m<sup>2</sup> in Fig. 11) did not change significantly the compressive strength, although the reduction in load after the maximum was faster as a result of the easy propagation of the cracks along particle/matrix interface. Thus, it can be concluded that the effect of the interface fracture energy on the transverse compressive strength of fiber-reinforced polymers is negligible, as compared with the influence of the interface strength.



#### 4.4 Influence of the matrix friction angle

The stress-strain curves under transverse compression of one RVE are plotted in Figs. 12(a), 12(b) and 12(c) for three composites with matrix friction angles of  $0^\circ$ ,  $15^\circ$  and  $30^\circ$ , respectively. As the matrix tensile strength was assumed to be constant and equal to 60 MPa, changes in the friction angle modified the yield strength of the matrix in compression — as given in equation (13) — which increased from 60 MPa ( $\phi = 0^\circ$ ) up to 180 MPa ( $\phi = 30^\circ$ ). So the stresses in Fig. 12 were normalized by the corresponding yield strength of the matrix in compression to compare the composite behavior on the same basis. The curves in Fig. 12(a) ( $\phi = 0^\circ$ ) are representative of a metallic matrix, which follows the Tresca yield criterion, while those in Figs. 12(b) and (c) stand for the behavior of polymeric matrices which tend to form shear bands oriented at an angle of  $45^\circ + \phi/2$  with the plane perpendicular to the compression axis. In the absence of interface decohesion, the matrix with  $\phi = 0^\circ$  provided the highest compressive strength (relative to the  $\sigma_{mc}$ ), and  $Y_C/\sigma_{mc}$  decreased progressively with the friction angle. This behavior is the result of the trend to localize the deformation in shear bands between the fibers, which increases with the friction angle. This effect was more marked in presence of interface decohesion, because matrix shear bands were triggered at lower strains by the stress concentrations around the interface cracks (Fig. 9a). Obviously, this mechanism is more efficient if the matrix friction angle is high, and thus the degradation of the composite properties was faster as the interfacial strength decreased.

#### 4.5 Influence of the thermal residual stresses

Residual stresses develop in PMC upon cooling at ambient temperature after curing as a result of the thermal expansion mismatch between the matrix and fibers. As the thermal expansion coefficient of the epoxy matrix is much higher than that of the fibers, tensile stress appears in the matrix and compressive in the fibers, and their influence on the behavior under transverse compression can be taken into account in the micromechanical model by simulating the composite behavior in two steps. In the first step, the RVE was subjected to a homogeneous temperature change of  $-100^\circ\text{C}$  from the stress-free temperature down to ambient temperature (38). The computational model and the fiber and matrix properties were those given in section 3 but the analyses were carried out under generalized plane strain conditions, instead of plane strain. The thickness of the model (perpendicular to the  $X_1 - X_2$ ) is constant in plane strain simulations, and this leads to unrealistic values of the thermal residual stresses along the  $X_3$  axis. Conversely, the generalized plane strain theory assumes that the model lies between two parallel planes which can move with

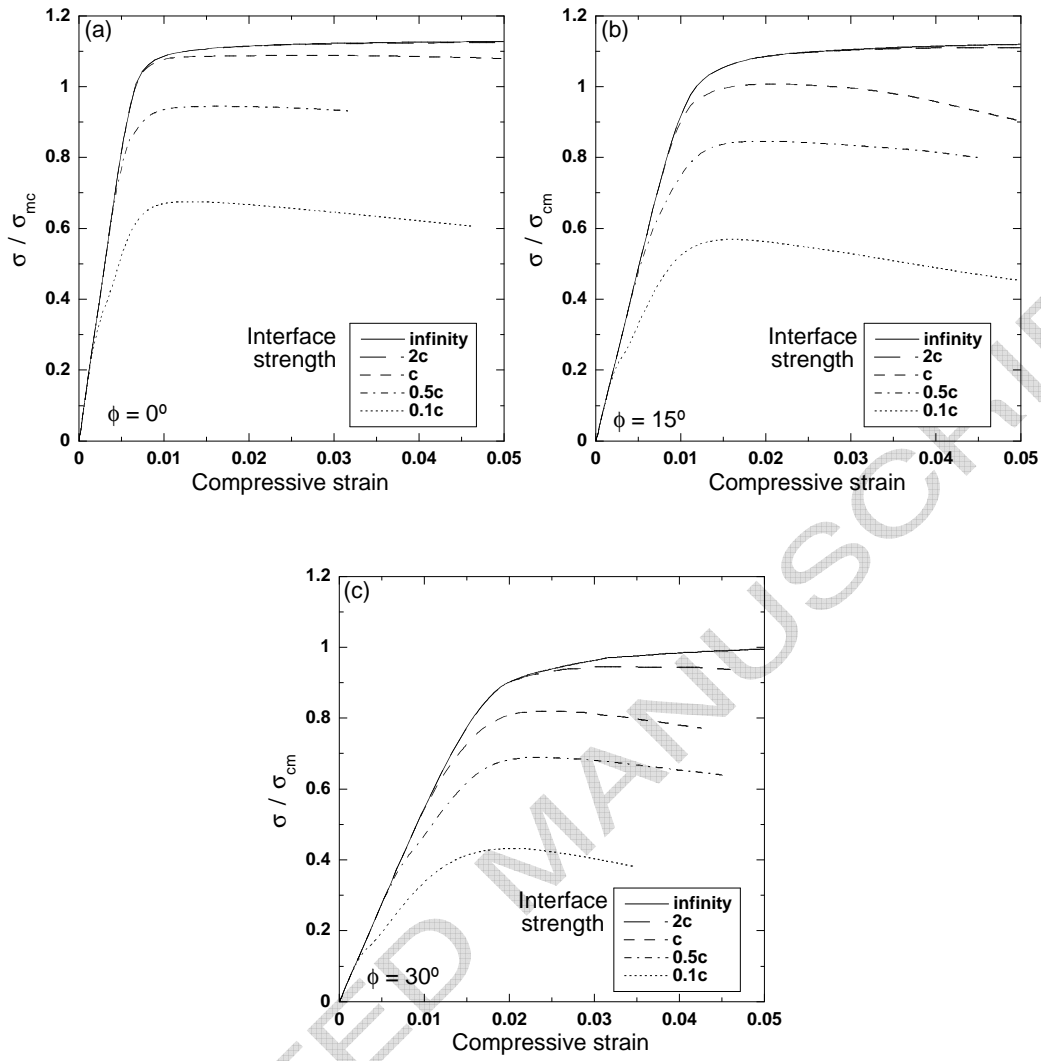


Fig. 12. Influence of the matrix friction angle on the stress-strain curve under transverse compression. (a)  $\phi = 0^\circ$ . (b)  $\phi = 15^\circ$ . (c)  $\phi = 30^\circ$ . The stresses are normalized by the respective strength of the matrix in compression.

respect to each other and can accommodate the thermal strain induced by the temperature change. Once the residual stresses were generated, the thickness along the  $X_3$  axis was held constant and the RVE was deformed under uniaxial compression. The stress-strain curves with and without residual stresses of one RVE are plotted in Fig. 13 for different values of the interface strength. The matrix and fiber properties correspond to those of the materials in Fig. 6. The non-linear deformation started at lower strains in the presence of residual stresses, but the compressive strength was not affected because the thermo-elastic residual stresses were rapidly smoothed out during deformation by the intense plastic deformation in the matrix and the interface cracks.

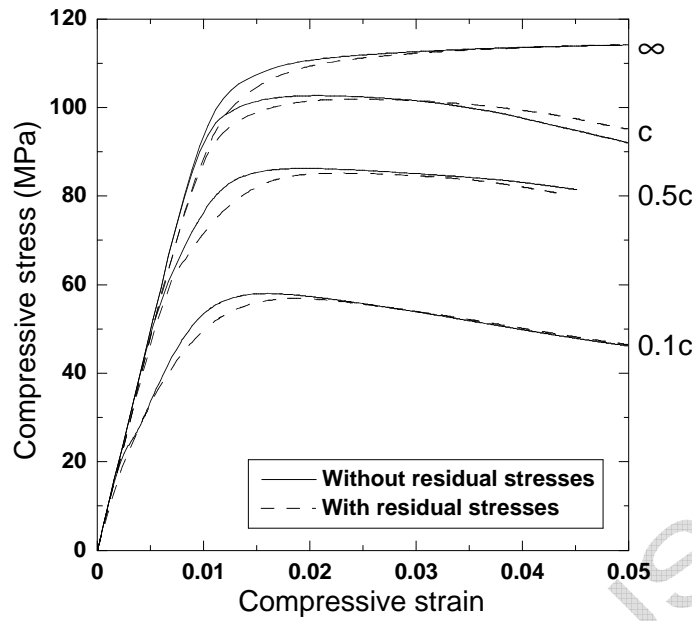


Fig. 13. Influence of the thermal residual stresses on the mechanical response under transverse compression for different values of the interface strength.

## 5 Conclusions

The compressive strength under transverse loading of fiber-reinforced polymers was studied by means of computational micromechanics. In this modeling strategy, the stress-strain curve was computed by means of the finite element analysis of an RVE of the composite microstructure. The simulations showed the role played by the two dominant damage mechanisms (decohesion at the interface and shear band formation in the matrix) in controlling the composite strength. On the one hand, if decohesion is inhibited, failure took place by the development of shear bands in the matrix, which propagated through the microstructure at an angle of  $\pm(45^\circ + \phi/2)$  with respect to the plane perpendicular to the compression axis. The compressive strength was slightly higher than the matrix strength under uniaxial compression due to the additional strengthening provided by the stiff fibers. On the other hand, interface cracks were nucleated at very low stresses in composites with weak interfaces, while the matrix was still in the elastic regime. The stress concentrations at the interface crack tips nucleated plastic shear bands between neighboring cracks, and led to the evolution of the cracks into large interfacial voids. Final fracture occurred by the development of bands of localized deformation formed by interfacial voids linked by matrix shear bands, the orientation of these bands being controlled by the particular distribution of the fibers in the RVE. When the interface strength was similar to the matrix

flow stress in compression ( $N \approx c$ ), the numerical simulation showed that the maximum strength was mainly controlled by the matrix, and coincided with the formation of an incipient pattern of shear bands in the matrix, inclined at  $\pm(45^\circ + \phi/2)$  with respect to the plane perpendicular to the compression axis. Final fracture took place thereafter by the propagation of a dominant shear band, slightly misoriented with respect to the theoretical angle, whose path was dictated by the linking up of interface cracks in adjacent fibers.

Parametrical studies showed that other factors (such as the matrix friction angle, the interface fracture energy and the thermo-elastic residual stresses) exerted a secondary influence on the compressive strength of PMC under transverse compression. The matrix was more susceptible to the formation of shear bands as the friction angle increased, and they developed earlier, but this effect was offset by the higher matrix flow stress in compression. Thermal residual stress reduced the stress for the onset of nonlinear deformation but they were rapidly smoothed out by the intense plastic deformation in the matrix and did not modify the compressive strength. Finally, changes in the interface fracture energy by two orders of magnitude did not modify significantly the compressive strength either.

It is finally worth noting the potential of computational micromechanics to assess the mechanical behavior of engineering composites. By using the appropriate constitutive equations for the fiber, matrix and interfaces, this simulation tool can provide a detailed picture of deformation and fracture mechanisms at microscopic level, including the effect of all non-linear processes and of the interaction among them. This information can be used to develop more accurate and reliable failure criteria at the lamina level, which in turn can be used to predict the mechanical performance of laminates and composite structures.

## 6 Acknowledgments

This investigation was supported by the Spanish Ministry of Education and Science through the grant MAT 2006-2602 and by the Comunidad de Madrid through the program ESTRUMAT-CM (reference MAT/0077).

## References

- [1] J. Aveston, G. A. Cooper, A. Kelly, Single and multiple fracture, in: *The Properties of Fibre Composites*, IPC Science and Technology Press, 1971, pp. 15–26.
- [2] W. A. Curtin, N. Takeda, Tensile strength of fiber-reinforced compos-

- ites: II. application to polymer matrix composites, *Journal of Composite Materials* 32 (1998) 2060–2081.
- [3] C. González, J. LLorca, Micromechanical modelling of deformation and failure in Ti-6Al-4V/SiC composites, *Acta Materialia* 49 (2001) 3505–3519.
  - [4] A. S. Argon, Fracture of composites, in: H. Herman (Ed.), *Treatise on Materials Science and Technology*, vol. 1, Academic Press, 1972, pp. 79–114.
  - [5] B. Budiansky, N. A. Fleck, Compressive failure of fiber composites, *Journal of the Mechanics and Physics of Solids* 41 (1993) 183–211.
  - [6] T. J. Vogler, S.-Y. Hsu, S. Kyriakides, Composite failure under combined compression and shear, *International Journal of Solids and Structures* 37 (2000) 1765–1791.
  - [7] J. C. Michel, H. Moulinec, P. Suquet, Effective properties of composite materials with periodic microstructure: a computational approach, *Computational Methods in Applied Mechanical Engineering* 172 (1999) 109–143.
  - [8] H. R. Lusti, P. J. Hine, A. A. Gusev, Direct numerical predictions for the elastic and thermoelastic properties of short fibre composites, *Composites Science and Technology* 62 (2002) 1927–1934.
  - [9] J. Segurado, J. LLorca, A numerical approximation to the elastic properties of sphere-reinforced composites, *Journal of the Mechanics and Physics of Solids* 50 (2002) 2107–2121.
  - [10] C. González, J. Segurado, J. LLorca, Numerical simulation of elastoplastic deformation of composites: Evolution of stress microfields and implications for homogenization models, *Journal of the Mechanics and Physics of Solids* 52 (2004) 1573–1593.
  - [11] N. Chawla, R. S. Sidhu, V. V. Ganesh, Three-dimensional visualization and microstructure-based modeling of deformation in particle-reinforced composites, *Acta Materialia* 54 (2006) 1541–1548.
  - [12] J. Segurado, C. González, J. LLorca, A numerical investigation of the effect of particle clustering on the mechanical properties of composites, *Acta Materialia* 51 (2003) 2355–2369.
  - [13] J. Segurado, J. LLorca, Computational micromechanics of composites: the effect of particle spatial distribution, *Mechanics of Materials* 38 (2006) 873–883.
  - [14] H. J. Böhm, W. Han, A. Eckschlager, Multi-inclusion unit cell studies of reinforcement stresses and particle failure in discontinuously reinforced ductile matrix composites, *Computer Modeling in Engineering & Sciences* 5 (2004) 5–20.
  - [15] J. LLorca, J. Segurado, Three-dimensional multiparticle cell simulations of deformation and damage in sphere-reinforced composites, *Materials Science and Engineering A365* (2004) 267–274.
  - [16] S. Youssef, E. Maire, R. Gaertner, Finite element modelling of the actual structure of cellular materials determined by X-ray tomography, *Acta*

- Materialia 53 (2005) 719–730.
- [17] A. Borbély, P. Kenesei, H. Biermann, Estimation of the effective properties of particle-reinforced metalmatrix composites from microtomographic reconstructions, *Acta Materialia* 54 (2006) 2735–2744.
  - [18] C. González, J. LLorca, Multiscale modeling of fracture in fiber-reinforced composites, *Acta Materialia* 54 (2006) 4171–4181.
  - [19] C. González, J. LLorca, Numerical simulation of the fracture behavior of Ti/SiC composites between 20°C and 400°C, *Metallurgical and Materials Transactions A* 38 (2007) in press.
  - [20] T. A. Collings, Transverse compressive behaviour of unidirectional carbon fibre reinforced plastics, *Composites* 5 (1974) 108–116.
  - [21] S. T. Pinho, L. Iannucci, P. Robinson, Physically-based failure models and criteria for laminated fibre-reinforced composites with emphasis on fibre-kinking. Part I: development, *Composites: Part A* 37 (2006) 63–73.
  - [22] Y. K. Huang, P. H. Frings, E. Hennes, Mechanical properties of Zylon/epoxy composite, *Composites: Part B* 33 (2002) 109–115.
  - [23] A. Puck, H. Schürmann, Failure analysis of frp laminates by means of physically based phenomenological models, *Composites Science and Technology* 62 (2002) 1633–1662.
  - [24] D. Aragonés, Fracture micromechanisms in C/epoxy composites under transverse compression, Master Thesis, Universidad Politécnica de Madrid, 2007.
  - [25] T. J. Vogler, S. Kyriakides, Inelastic behavior of an AS4/PEEK composite under combined transverse compression and shear. Part I: experiments, *International Journal of Plasticity* 15 (1999) 783–806.
  - [26] H. M. Hsiao, I. M. Daniel, Strain rate behavior of composite materials, *Composites: Part B* 29 (1998) 521–533.
  - [27] A. J. Kinloch, R. J. Young, *Fracture Behavior of Polymers*, Elsevier Applied Science, 1983.
  - [28] Z. Hashin, Failure criteria for unidirectional fiber composites, *Journal of Applied Mechanics* 47 (1980) 329–334.
  - [29] J. Segurado, J. LLorca, A new three-dimensional interface finite element to simulate fracture in composites, *International Journal of Solids and Structures* 41 (2004) 2977–2993.
  - [30] J. Segurado, J. LLorca, A computational micromechanics study of the effect of interface decohesion on the mechanical behavior of composites, *Acta materialia* 53 (2005) 4931–4942.
  - [31] F. Hashagen, R. de Borst, Numerical assessment of delamination in fibre metal laminates, *Computational Methods in Applied Mechanical Engineering* 185 (2000) 141–159.
  - [32] S. Ghosh, Y. Ling, B. Majumdar, R. Kim, Interfacial debonding analysis in multiple fiber reinforced composites, *Mechanics of Materials* 32 (2000) 561–591.
  - [33] J. R. Brockenbrough, S. Suresh, H. A. Wienecke, Deformation of metal-matrix composites with continuous fibers: geometrical effects of fiber dis-

- tribution and shape, *Acta Metallurgica et Materialia* 39 (1991) 735–752.
- [34] P. J. Hine, H. R. Lusti, A. A. Gusev, Numerical simulation of the effects of volume fraction, aspect ratio and fibre length distribution on the elastic and thermoelastic properties of short fibre composites, *Composites Science and Technology* 62 (2002) 1445–1453.
  - [35] Abaqus, Users' Manual, ABAQUS, Inc., 2006.
  - [36] P. Suquet, Effective properties of nonlinear composites, in: *Continuum Micromechanics. CISM Course and Lecture Notes*, 1997, pp. 197–264.
  - [37] S. Hazanov, C. Huet, Order relationships for boundary condition effects in heterogeneous bodies smaller than the representative volume, *Journal of the Mechanics and Physics of Solids* 42 (1994) 1995–2011.
  - [38] P. D. Soden, M. J. Hinton, A. S. Kaddour, Lamina properties, lay-up configurations and loading conditions for a range of fibre-reinforced composite laminates, *Composites Science and Technology* 58 (1998) 1011–1022.
  - [39] Abaqus, Theory Manual, HKS, Inc., 1998.
  - [40] P. Menetrey, K. J. Willam, Triaxial failure criterion for concrete and its generalization, *ACI Structural Journal* 92 (1995) 311–318.
  - [41] X.-F. Zhou, H. D. Wagner, S. R. Nutt, Interfacial properties of polymer composites measured by push-out and fragmentation tests, *Composites: Part A* 32 (2001) 1543–1551.
  - [42] Z. F. Khisaeva, M. Ostoj-Starzewski, On the size of RVE in finite elasticity of random composites, *Journal of Elasticity* 85 (2006) 153–173.
  - [43] M. J. Pitkethly, *et al.*, A round robin programme on interfacial test methods, *Composites Science and Technology* 48 (1993) 205–214.
  - [44] K. Benzarti, L. Cangemi, F. D. Maso, Transverse properties of unidirectional glass/epoxy composites: influence of fibre surface treatments, *Composites: Part A* 32 (2001) 197–206.